



HAL
open science

Effect of defect size and shape on the high-cycle fatigue behavior

Raphaël Guerchais, Franck Morel, Nicolas Saintier

► **To cite this version:**

Raphaël Guerchais, Franck Morel, Nicolas Saintier. Effect of defect size and shape on the high-cycle fatigue behavior. *International Journal of Fatigue*, 2017, 100, pp.530-539. hal-02332159

HAL Id: hal-02332159

<https://hal.science/hal-02332159v1>

Submitted on 24 Oct 2019

HAL is a multi-disciplinary open access archive for the deposit and dissemination of scientific research documents, whether they are published or not. The documents may come from teaching and research institutions in France or abroad, or from public or private research centers.

L'archive ouverte pluridisciplinaire **HAL**, est destinée au dépôt et à la diffusion de documents scientifiques de niveau recherche, publiés ou non, émanant des établissements d'enseignement et de recherche français ou étrangers, des laboratoires publics ou privés.

Effect of defect size and shape on the high-cycle fatigue behavior

R. Guerchais^{a,*}, F. Morel^a, N. Saintier^b

^aArts et Metiers ParisTech, LAMPA, 2 bd du Ronceray, 49035 Angers Cedex, France

^bArts et Metiers ParisTech, I2M – UMR CNRS 5295, Université Bordeaux 1, Esplanade des Arts et Métiers, 33405 Talence Cedex, France

Keywords:

High-cycle fatigue
Elliptical notch
Crystal plasticity
Micromechanics
Fatigue criteria

A B S T R A C T

This study aims to examine the effects of both material microstructure and voids on the high-cycle fatigue behavior of metals. To deal with this matter, finite element analyses of polycrystalline aggregates are carried out, for different configurations of crystalline orientations, in order to estimate the mechanical state, at the grain scale, in the vicinity of a small elliptical hole. Fatigue criteria are then applied to estimate the average fatigue limit in fully reversed tension, for different defect sizes and ellipse aspect ratios. The constitutive models and the fatigue criteria are calibrated using experimental data obtained from specimens made of 316L austenitic steel. The estimations are then compared with the experimental trends.

1. Introduction

The high-cycle fatigue strength of metallic materials is strongly influenced by the microstructure and may be significantly affected by the presence of defects, and it is thus important to be able to quantify their detrimental effect. A large number of approaches attempting to predict the influence of a defect on the fatigue limit can be found in the literature. For instance, Kitagawa and Takahashi have proposed a criterion based on a linear elastic fracture mechanic threshold [1]. Shyam et al. have extended this approach by considering an elastic plastic fracture mechanic threshold [2]. Empirical fatigue criteria have been proposed by Frost [3] and Murakami and Endo [4]. Endo and McEvily have developed a criterion relying on the fatigue crack propagation [5]. The gradient of a fatigue equivalent stress, inspired by classical multiaxial fatigue criteria such as the Crossland criterion [6], has been used by Nadot and his coworkers [7–9].

Among these approaches, the one proposed by Murakami and Endo is based on the defect size \sqrt{area} , expressed by the square root of the area of the defect projected in the direction of the maximum principal stress, which is a crucial parameter to determine the fatigue strength [4]. Billaudeau et al. have shown, from push-pull fatigue tests carried out on specimens made of low carbon steel (SAE1035) and containing an artificial notch, that the fatigue limit is affected not only by the size of the defect \sqrt{area} but also by

its morphology [10]. More precisely, the authors have highlighted that, for a given defect size area, an increase in the stress concentration factor K_t of the defect:

- induces a significant decrease in the fatigue strength when $K_t \in [1; 2]$,
- leads to a slight increase in the fatigue limit when $K_t \in [2; +\infty[$ (see Fig. 1).

The increase of the fatigue strength with the increase of the stress concentration factor K_t , observed when $K_t \in [2; +\infty[$, is a counter-intuitive experimental trend which has still been little discussed. Moreover, too few predictions of fatigue criteria has been confronted to these data.

The objective of the present work is to analyze this issue from a numerical point of view, in the continuation of previous works [11–13] where fatigue design methodologies based on finite element analyses (FEA) of polycrystalline microstructures have been proposed. More precisely, FEAs of two-dimensional polycrystalline aggregates, loaded in fully reversed tension, are conducted in order to estimate the mechanical behavior, at the grain scale, in microstructures containing a small elliptical hole. Two fatigue criteria are then calibrated by employing the results of the FEA and experimental data obtained from fatigue tests conducted on specimens, made of 316L austenitic steel, with and without a hemispherical notch [12]. The estimations of these criteria for different defect sizes and ellipse aspect ratios are compared to the experimental trends.

* Corresponding author.

E-mail address: raphael.guerchais@ensam.eu (R. Guerchais).

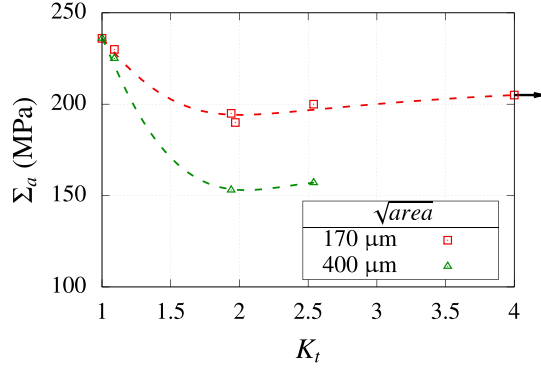


Fig. 1. Fatigue limits of SAE1035 steel as a function of the stress concentration K_t for different defect sizes $\sqrt{\text{area}}$ [10].

2. Polycrystalline aggregate model

2.1. Finite element model of the polycrystalline aggregates

The geometry of the polycrystal is defined by a partition of a two-dimensional square-shaped domain into convex polygonal subdomains obtained through a Voronoi decomposition. Due to the sizes chosen for the polycrystal (see Fig. 2), 3265 seeds are used in the Voronoi tessellation so that the mean grain size in the numerical model corresponds to the mean grain size of the material tested [12], i.e. 14 μm . The geometry of the polycrystal is then regularized by deleting small geometric entities (edges and arcs of ellipses) to prevent unreasonable mesh refinement. The microstructure obtained following the regularization process is illustrated in Figs. 2 and 3.

In addition to the polycrystal, an elastic-plastic homogeneous matrix is modeled in order to avoid applying the boundary conditions directly on the edges of the microstructure. The model is loaded in fully reversed uniaxial tension along the y-direction thanks to a homogeneous stress field applied on the upper and lower edges of the matrix. The loading sequence, describing the evolution of the macroscopic axial stress $\Sigma_{yy}(t)$ applied on the matrix, is defined in Eq. (1):

$$\Sigma_{yy}(t) = \begin{cases} \Sigma_{yy,a} t & \forall t \in [0; 1[\\ \Sigma_{yy,a} \cos(2\pi t) & \forall t \in [1; 4] \end{cases} \quad (1)$$

The defect assumed in this study is an elliptical hole characterized by its length $2a$ in the x-direction and its length $2b$ in the y-direction. Three values of the defect size $2a$ (95 μm , 365 μm and 510 μm) and three values of ellipse aspect ratio b/a (0.5, 1.0 and 1.5) are examined (see Fig. 3).

The orientation of the crystal coordinate system of each grain, with respect to the reference frame of the polycrystal, is characterized by three angles called Euler angles. Ten orientation sets, made up of 3265 triplets of Euler angles selected to be representative of the texture of the material tested [12], are used. Consequently, the response of 10 different realizations of microstructure is analyzed per defect size. The mesh generator Gmsh [14] is used to discretize the geometries with three-node triangular elements. Each grain is discretized in average with 14 elements, and a generalized plane strain hypothesis is adopted.

2.2. Constitutive model of the single crystal

Due to the face-centered cubic lattice of the austenitic crystals, the elastic behavior is described by a linear cubic elasticity model characterized by three material parameters C_{1111} , C_{1122} and C_{1212} defined in the crystal coordinate system. The values of these parameters, calibrated for a Fe-18Cr-14Ni steel by Teklu et al. [15], are given in Table 1. The constitutive model used to describe the single crystal viscoplastic behavior of the crystals comes from the work of Méric et al. [16]. In this model, the plastic slip, which occurs along the close-packed lattice planes $\{111\}$ in the close-packed directions $[\bar{1}10]$, is described for each slip system s with the following flow rule:

$$\dot{\gamma}_s = \left\langle \frac{|\tau_s - \chi_s| - r_0 - r_s}{K} \right\rangle_+^n \text{sgn}(\tau_s - \chi_s) = \dot{\gamma}_s \text{sgn}(\tau_s - \chi_s) \quad (2)$$

where τ_s is the resolved shear stress acting on the slip system s , r_0 is the initial critical shear stress, χ_s and r_s are respectively the kinematic and isotropic hardening variables associated to the slip system s , K and n are the parameters controlling the viscosity. The

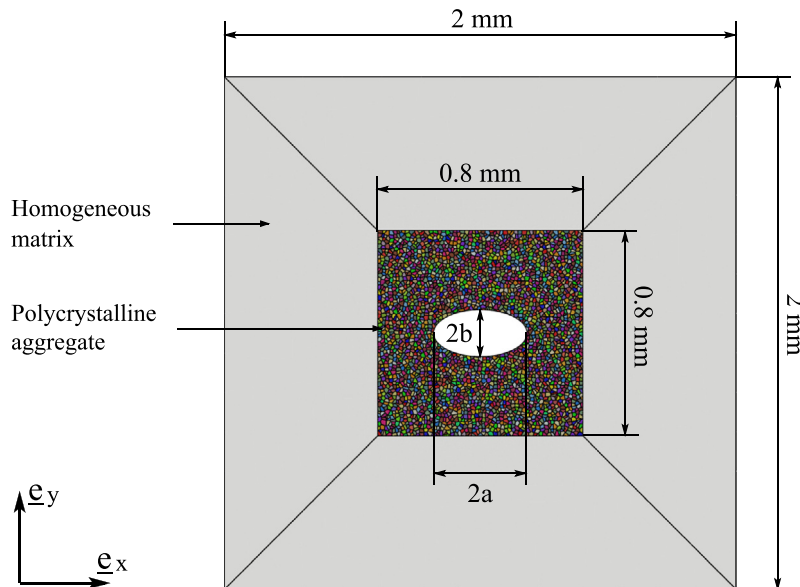


Fig. 2. Shape and sizes of the polycrystalline aggregate and the homogeneous matrix used in the finite element analysis.

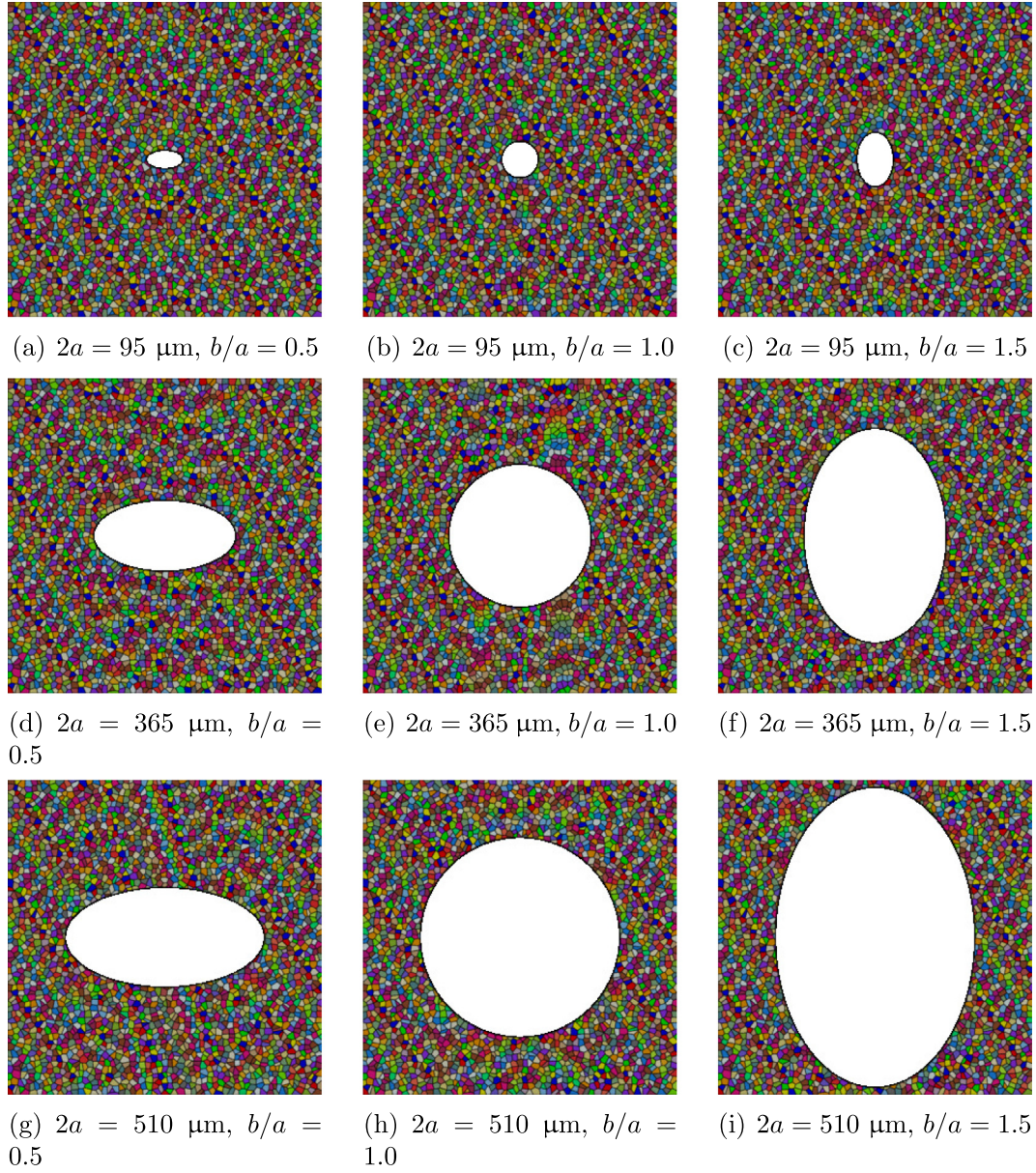


Fig. 3. Illustration of the different configurations of the elliptical notch studied.

Table 1
Material parameters of the single crystal constitutive model for a 316L steel.

| Cubic elasticity | | | Viscosity | | Kinematic hardening | | | |
|---------------------|------------------|------------------|-------------------------------|-------|---------------------|-------------------|-------|-------|
| C_{1111} (GPa) | C_{1122} (GPa) | C_{1212} (GPa) | K (MPa · s ^{1/n}) | n | c (MPa) | d | | |
| 198 | 125 | 122 | 10 | 10 | $2.04 \cdot 10^5$ | $3.63 \cdot 10^3$ | | |
| Isotropic hardening | | | | | | | | |
| r_0 (MPa) | Q (MPa) | b | h_0 | h_1 | h_2 | h_3 | h_4 | h_5 |
| 87.0 | 1.06 | 4.88 | 1 | 1 | 0.438 | 77.2 | 4.31 | 2.41 |

resolved shear stress τ_s acting on the slip system s , characterized by a unit vector normal to the slip plane \underline{n}_s and a unit vector collinear to the slip direction \underline{l}_s , can be computed from the stress tensor $\underline{\underline{\sigma}}$ as follows:

$$\tau_s = \left(\frac{\underline{n}_s \otimes \underline{l}_s + \underline{l}_s \otimes \underline{n}_s}{2} \right) : \underline{\underline{\sigma}} \quad (3)$$

Non-linear hardening rules are used to describe the isotropic hardening variable r_s and the kinematic hardening variable χ_s :

$$r_s = Q \sum_r h_{sr} (1 - e^{-b v_r}) \quad (4)$$

$$\dot{\chi}_s = c \dot{\gamma}_s - d \dot{v}_s \chi_s \quad (5)$$

Table 2

Material parameters of the macroscopic constitutive model for a 316L steel.

| Isotropic elasticity | | Yield stress | Isotropic hardening | | Kinematic hardening | |
|----------------------|-------|------------------|---------------------|------|---------------------|-------------------|
| E (GPa) | ν | σ^y (MPa) | Q_∞ (MPa) | B | C (MPa) | γ |
| 194 | 0.284 | 129 | 142 | 6.88 | $7.05 \cdot 10^5$ | $3.08 \cdot 10^3$ |

The material parameters of the single crystal viscoplasticity model have been calibrated from low-cycle fatigue tests conducted in several loading conditions: tension, torsion and combined out-of-phase tension and torsion [13]. These parameters are summarized in Table 1.

2.3. Constitutive model of the homogeneous matrix

The elastic behavior of the homogeneous matrix is described by a linear isotropic elasticity model characterized by the Young's modulus E and the Poisson's ratio ν . The rate-independent plasticity model is defined by a von Mises yield function:

$$f = \sqrt{\frac{3}{2} (\underline{\underline{\sigma}}^d - \underline{\underline{X}}^d) : (\underline{\underline{\sigma}}^d - \underline{\underline{X}}^d)} - \sigma^y - R \quad (6)$$

with σ^y , $\underline{\underline{\sigma}}$, $\underline{\underline{X}}$ and R corresponding respectively to the initial yield stress, the stress tensor, the backstress tensor and the isotropic hardening variable. The superscript \bullet^d indicates the deviatoric part of a given tensor. The non-linear functions describing the rates of the isotropic hardening variable R and of the backstress tensor $\underline{\underline{X}}$ are defined by Eqs. (7) and (8):

$$\dot{R} = B(Q_\infty - R)\dot{p} \quad (7)$$

$$\dot{\underline{\underline{X}}} = \frac{2}{3} C \dot{\underline{\underline{\epsilon}}}^p - \gamma \underline{\underline{X}} \dot{p} \quad (8)$$

In Eqs. (7) and (8), p and $\underline{\underline{\epsilon}}^p$ denote the equivalent plastic strain and the plastic strain tensor respectively, whereas Q_∞ , B , C and γ are material parameters. The set of such parameters of this elastic-plastic constitutive model has been calibrated for a 316L steel [12] and are given in Table 2.

3. Analysis of the mechanical responses in the polycrystals

The mechanical responses are analyzed in high-cycle fatigue conditions. Therefore, the loading amplitudes applied to the microstructures are closed to the presumed average fatigue limits. The amplitudes of the macroscopic axial stress $\Sigma_{yy,a}$, which have been selected, are presented in Table 3.

The analysis of the mechanical responses in the polycrystals focuses first on the local mechanical quantities computed at the gauss point. The effect of the anisotropy of the local behavior added to the variability of the crystalline orientations on the distribution of the stress in the vicinity of the elliptical notch is analyzed. Then, some mesoscopic mechanical quantities, i.e. mechanical quantities computed from the stress tensor averaged per grain, obtained during the last loading cycle and related to the fatigue criteria presented in the following section, are discussed.

3.1. Local mechanical responses

The von Mises equivalent stress fields obtained during the final time step of FEA are illustrated in Fig. 4 to give a brief overview of the main characteristics of the local mechanical fields. The microstructures shown in this figure contain an elliptical notch with a defect $2a = 365 \mu\text{m}$ and different aspect ratios b/a : 0.5 in

Table 3Amplitude of the macroscopic axial stress $\Sigma_{yy,a}$ applied to the matrix, for each defect size $2a$ studied.

| $2a$ (μm) | 0 | 95 | 365 | 510 |
|------------------------|-------|-------|-------|-------|
| $\Sigma_{yy,a}$ (MPa) | 232.5 | 212.5 | 180.0 | 152.5 |

the 1st column, 1.0 in the 2nd column, and 1.5 in the 3rd column. The results obtained for two different sets of crystalline orientations are displayed in each row.

It can be observed that the anisotropy of the behavior of the single crystals induces a heterogeneous stress field in addition to the stress gradient caused by the elliptical notches. As was expected, the ranges and the maximum values of the von Mises stress increase with the decrease of the curvature radius $\rho = b^2/a$ in the critical regions of the ellipse and, thus, with the decrease of the ellipse aspect ratio b/a . Moreover, the configuration of the crystalline orientations in the microstructure affects the maximum values reached by the von Mises equivalent stress, but it also influences the location of the most stressed regions of the microstructures.

The distributions of the stress $\sigma_{yy}(t_f)$, along the line $y = 0$, obtained with a defect size $2a = 365 \mu\text{m}$, are plotted in Fig. 5, for the different ellipse aspect ratios b/a : 0.5 (red line), 1.0 (green line) and 1.5 (blue line). Each diagram " $\sigma_{yy}(t_f) - x$ " represents the results obtained with a given set of crystalline orientations. In these diagrams, the vertical dashed lines represent the positions of the intersections of the grain boundaries with the line $y = 0$.

From these example, it can be observed that the profiles of the axial stress $\sigma_{yy}(t_f)$ cannot be described by a monotonically decreasing function, unlike the solutions obtained in an isotropic elastic medium. For instance, in the upper left diagram, the stress levels in the second grain from the left are higher than those in the first grain which is on the elliptical notch. The stress concentration induced by the elliptical notch is partially responsible for the heterogeneity of the axial stress $\sigma_{yy}(t_f)$ but the anisotropy of the elastic-plastic behavior of the grains also contributes to this disparity. Indeed, far from the defect ($x \geq 100 \mu\text{m}$) the heterogeneity of the stress along the line $y = 0$ is almost exclusively due to the strain incompatibilities induced by the anisotropy of the local behavior.

In order to study the scatter of the mechanical response, induced by the variability of the crystalline orientations, the mean and the standard deviation of the stress $\sigma_{yy}(t_f)$, along the line $y = 0$, are displayed in Fig. 6. More precisely, the mean over ten orientation sets of the stress $\sigma_{yy}(t_f)$, along the line $y = 0$, is represented by dashed lines, for a defect size $2a = 365 \mu\text{m}$ and different ellipse aspect ratios b/a : 0.5 (red line), 1.0 (green line) and 1.5 (blue line). The standard deviation around the mean is represented by a pair of solid lines for each value of ellipse aspect ratio b/a .

As expected, the axial stress $\sigma_{yy}(t_f)$, in average on the ten realizations of microstructures, tends to decrease with the distance from the defect. The effect of the ellipse aspect ratio b/a on the distribution of the axial stress $\sigma_{yy}(t_f)$ is substantially perceptible up to

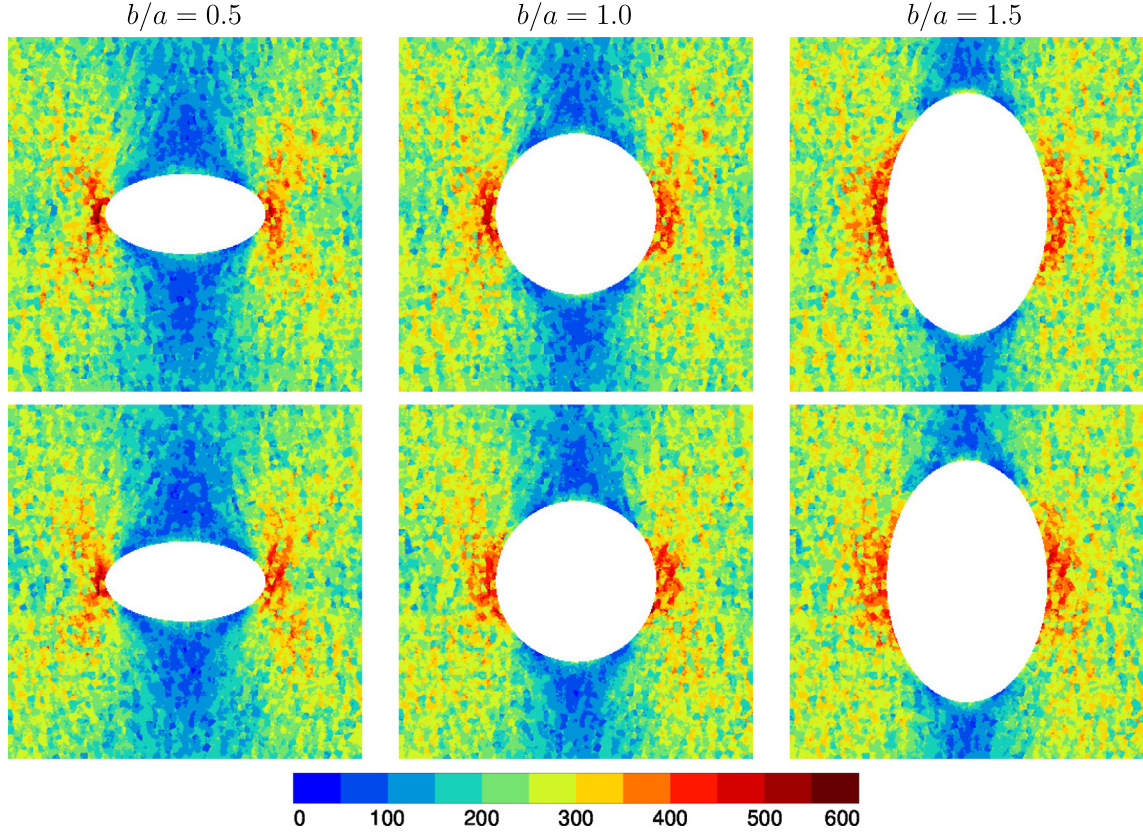


Fig. 4. Von Mises equivalent stress fields at the final time step t_f in microstructures containing an elliptical notch characterized by a defect size $2a = 365 \mu\text{m}$ for different ellipse aspect ratios b/a and different sets of crystalline orientations.

about $75 \mu\text{m}$. Indeed, beyond seven grains, the stress ranges vary similarly for the different notch shapes. It can also be observed that the microstructure does not have a negligible effect on the distribution of the axial stress $\sigma_{yy}(t_f)$. The ratio between the standard deviation and the mean of the axial stress $\sigma_{yy}(t_f)$ ranges from 0.05 to 0.2. Moreover, it's worth noting that the ranges and the standard deviations of the axial stress $\sigma_{yy}(t_f)$ are significantly larger in the vicinity of the notch root ($x \leq 100 \mu\text{m}$) than far from the stress concentration. These conclusions, discussed in the case of a defect sizes $2a = 365 \mu\text{m}$, hold true in the case of the other defect size studied.

3.2. Mesoscopic mechanical responses

Three mesoscopic mechanical quantities, assumed to be significant to characterize the HCF failure, are used in the fatigue criteria defined in the following section: the amplitude of the shear stress $\tau_a(\underline{n})$, the amplitude of the normal stress $\sigma_{n,a}(\underline{n})$, and the mean normal stress $\sigma_{n,m}(\underline{n})$, each acting on the slip plane defined by its unit normal vector \underline{n} (see [12] for the definitions of these mechanical quantities). Since the mean normal stresses $\sigma_{n,m}(\underline{n})$ are small in the case of stress ratio $R = \Sigma_{yy,\min}/\Sigma_{yy,\max} = -1$, compared to the amplitude of the shear stress $\tau_a(\underline{n})$ and the amplitude of the normal stress $\sigma_{n,a}(\underline{n})$, only these latter are discussed. The distribution of these mesoscopic mechanical quantities, in addition to their maximum values observed in each case, are shown respectively in Figs. 7 and 8.

It can be observed in Fig. 7 that the characteristics of the elliptical notch has a noticeable influence on the shape, in particular on the skewness, of the distribution of the shear stress amplitude τ_a .

The skewness of a sample can be measured by the adjusted Fisher-Pearson standardized moment coefficient G_1 defined as follows:

$$G_1 = \frac{N}{(N-1)(N-2)} \frac{\sum_{i=1}^N (x_i - \bar{x})^3}{s^3} \quad (9)$$

where N is the number of values in the sample, \bar{x} is the sample mean and s is the corrected sample standard deviation (Eq. (10)).

$$s = \sqrt{\frac{1}{N-1} \sum_{i=1}^N (x_i - \bar{x})^2} \quad (10)$$

The sample skewness G_1 increases with the decrease in ellipse aspect ratio b/a and with the increase in defect size $2a$. Moreover, this parameter is negative for defect-free microstructures and for microstructures containing a small defect ($2a = 95 \mu\text{m}$). The sign of the skewness becomes positive for large elliptical notch ($2a = 510 \mu\text{m}$). Contrary to the case of the shear stress amplitude τ_a , the overall shape of the distribution of the normal stress amplitude $\sigma_{n,a}$ is not significantly affected by the change of defect size $2a$ and ellipse aspect ratio b/a , at least, for the ranges of the defect sizes and aspect ratios studied.

The maximum values reached by both the shear stress amplitude τ_a and the normal stress amplitude $\sigma_{n,a}$ are dependent on the characteristic of the elliptical notch. Clear trends are observed in the case of the shear stress amplitude τ_a . First, when the loading amplitudes $\Sigma_{yy,a}$ are close to the fatigue limits, the maximum value reached by the shear stress amplitude τ_a increases with the increase in the defect size $2a$. Moreover, at a certain loading amplitude $\Sigma_{yy,a}$ and defect size $2a$, a decrease in the ellipse aspect ratio

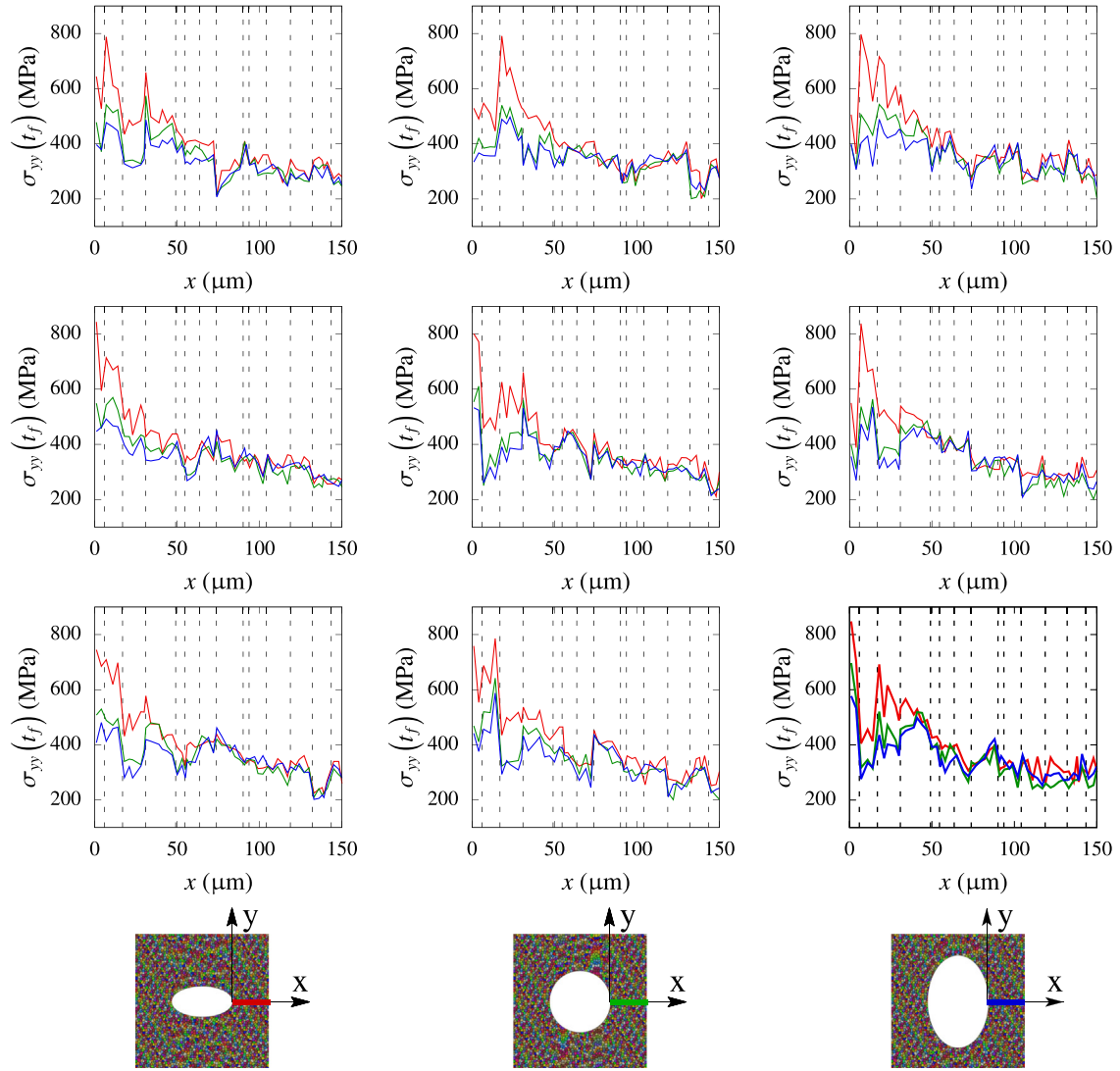


Fig. 5. Examples of the distributions, along the line $y = 0$, of the stress σ_{yy} at the final time step t_f of the FEA, with a defect size $2a = 365 \mu\text{m}$, for different ellipse aspect ratios b/a and sets of crystalline orientations.

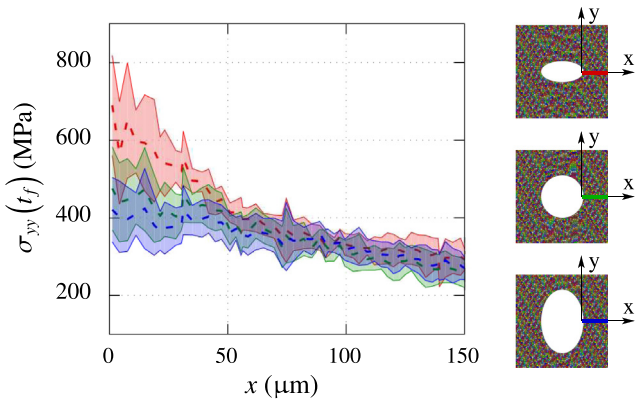


Fig. 6. Mean (dashed lines) and standard deviation around this mean (solid lines), for ten different orientation sets, of the stress $\sigma_{yy}(t_f)$, along the line $y = 0$, for a defect size $2a = 365 \mu\text{m}$ and for different ellipse aspect ratios b/a .

b/a leads to an increase in the maximum value of the shear stress amplitude τ_a . These conclusions are not necessarily valid in the case of the normal stress amplitude $\sigma_{n,a}$.

4. Fatigue analysis

4.1. Definition of the fatigue criteria

The determination of the macroscopic fatigue strength requires specific fatigue criteria to accurately estimate the detrimental effect of a small notch. In order to address this issue, two multiaxial fatigue criteria, previously discussed, are used in the present work:

- a probabilistic fatigue criterion based on a distribution of the crack initiation threshold [12],
- a deterministic criterion relying on a fatigue damage process zone [13].

Three mechanical quantities, computed from the mesoscopic stress tensors (i.e. the stress tensor averaged per grain) obtained during the last loading cycle of the FEA, are used in the definition of these fatigue criteria: the amplitude of the shear stress $\tau_a(\underline{n})$, the amplitude of the normal stress $\sigma_{n,a}(\underline{n})$, and the mean normal stress $\sigma_{n,m}(\underline{n})$, each acting on the slip plane of unit normal vector \underline{n} (see Ref. [12] for the definitions of these quantities).

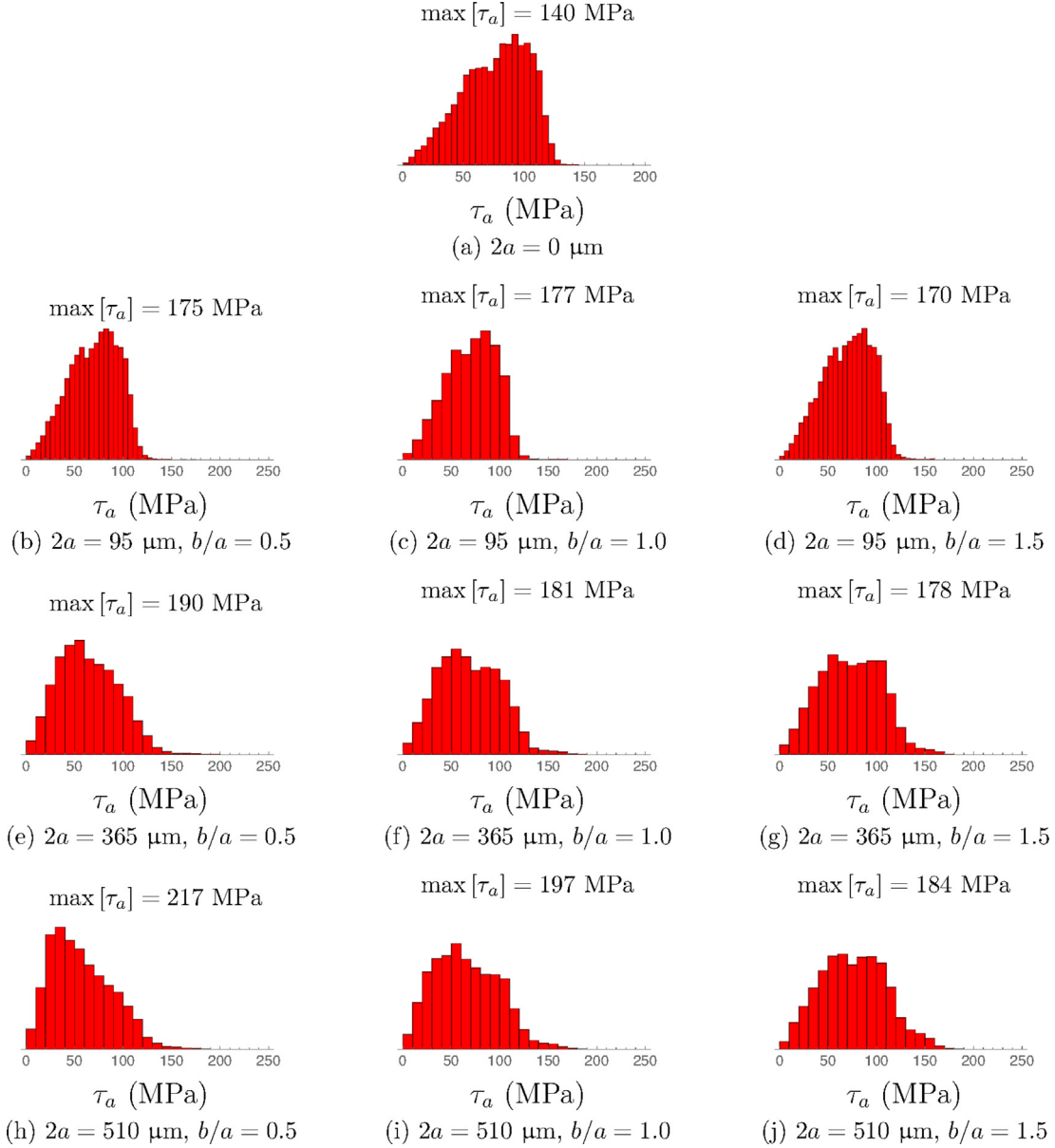


Fig. 7. Distribution of the shear stress amplitude τ_a in smooth polycrystalline aggregates and in polycrystalline aggregates containing an elliptical hole with different defect size $2a$ and ellipse aspect ratios b/a .

4.1.1. Probabilistic fatigue criterion

The probabilistic criterion, presented in [12], is based on the hypothesis that a fatigue crack initiates on the slip plane of unit normal vector \underline{n} if the amplitude of the shear stress $\tau_a(\underline{n})$ acting on this plane exceeds a threshold $\tau_a^{th}(\underline{n})$. Assuming that this threshold is a Weibull distributed random variable, the probability $P_{Fn}(\underline{n})$ that a fatigue crack initiation occurs on the slip plane is:

$$P_{Fn}(\underline{n}) = P(\tau_a(\underline{n}) \geq \tau_a^{th}(\underline{n})) = 1 - \exp\left[-\left(\frac{\tau_a(\underline{n})}{\tau_0(\underline{n})}\right)^m\right] \quad (11)$$

where $\tau_0(\underline{n})$ and m are respectively the scale and the shape parameters of the Weibull distribution. In order to account for the effect of the normal stress on the fatigue strength, the scale parameter $\tau_0(\underline{n})$ depends on the mean and the alternating part of the normal stress (respectively $\sigma_{n,m}(\underline{n})$ and $\sigma_{n,a}(\underline{n})$) as follows:

$$\tau_0(\underline{n}) = \tau'_0 \frac{1 - b\sigma_{n,m}(\underline{n})}{1 + a(\sigma_{n,a}(\underline{n})/\tau_a(\underline{n}))} \quad (12)$$

The failure probability of a grain P_{Fg} is then assumed to correspond to the maximum value, among the set of four slip planes \mathcal{A} , of the failure probability $P_{Fn}(\underline{n})$:

$$P_{Fg} = \max_{\underline{n} \in \mathcal{A}} [P_{Fn}(\underline{n})] \quad (13)$$

The weakest-link hypothesis, which means that the polycrystal fails when the weakest grain fails, is used in order to define the failure probability of a polycrystal P_{Fa} containing N_g grains:

$$1 - P_{Fa} = \prod_{g=1}^{N_g} (1 - P_{Fg}) \quad (14)$$

4.1.2. Deterministic fatigue criterion

The deterministic criterion discussed in this section has been presented in a previous study [13]. Summarily, this criterion relies on the assumption that the fatigue crack initiation occurs if an

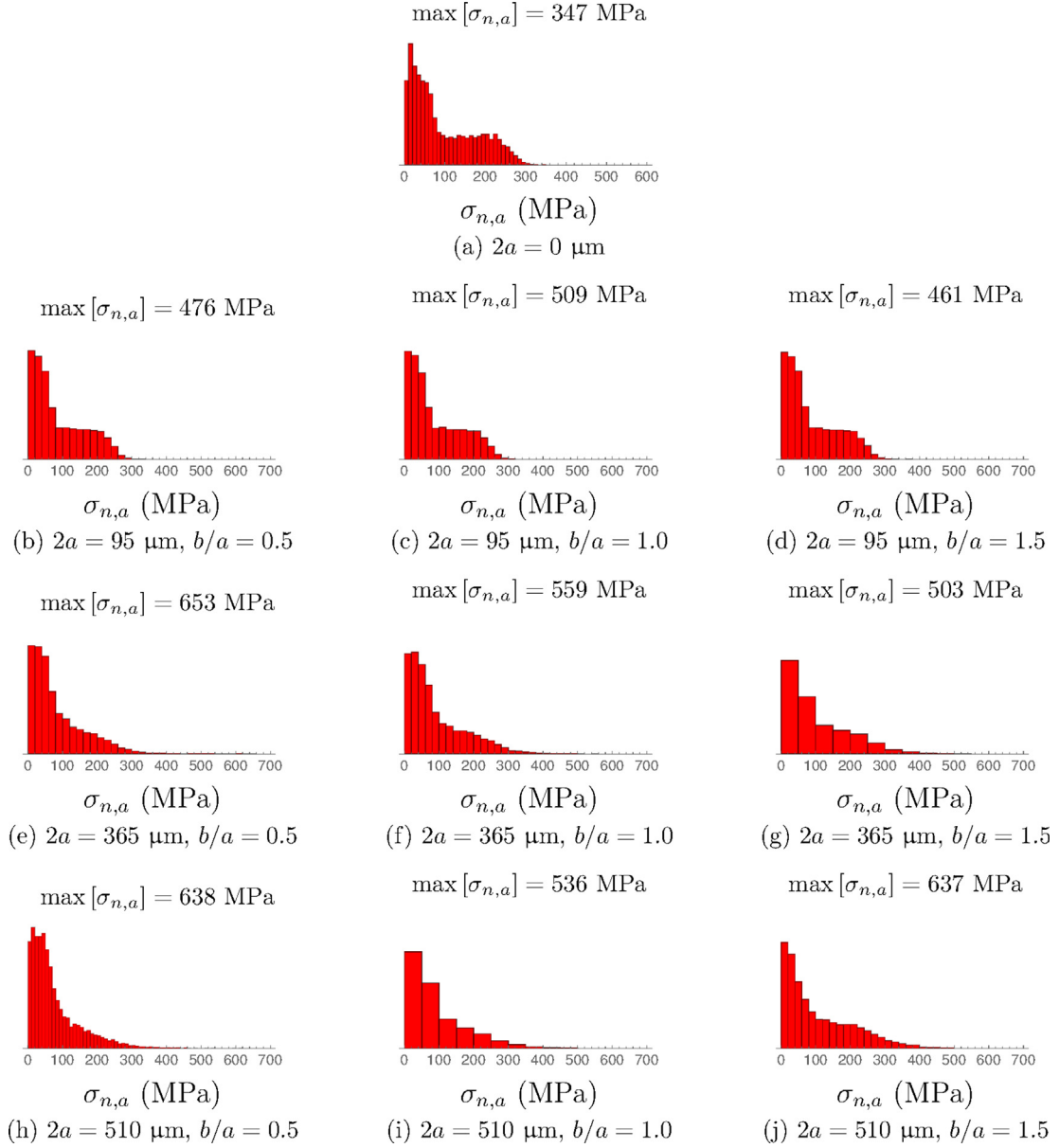


Fig. 8. Distribution of the normal stress amplitude $\sigma_{n,a}$ in smooth microstructures and in polycrystalline aggregates containing an elliptical hole with different defect size $2a$ and ellipse aspect ratios b/a .

equivalent stress σ_{eq} averaged over a given grain set G_{pZ} exceeds a threshold γ :

$$\sigma_{eq,w} = \sum_{g \in G_{pZ}} [f_g \sigma_{eq}] \geq \gamma \quad (15)$$

with f_g corresponding to the volume fraction of the grain g . The equivalent stress σ_{eq} is defined for each grain as the maximum value, among the set of four slip planes \mathcal{A} , of a linear combination of $\tau_a(\underline{n})$, $\sigma_{n,a}(\underline{n})$ and $\sigma_{n,m}(\underline{n})$:

$$\sigma_{eq} = \max_{\underline{n} \in \mathcal{A}} [\tau_a(\underline{n}) + \alpha \sigma_{n,a}(\underline{n}) + \beta \sigma_{n,m}(\underline{n})] \quad (16)$$

The grain set G_{pZ} , which can be seen as a fatigue damage process zone, is built in two steps. First, the grain with the highest value of equivalent stress σ_{eq} is determined. This critical grain constitutes the first element of the set G_{pZ} . Then, the grains included in the first N_n neighborhoods are added to the set G_{pZ} . A grain g is considered in the neighborhood n if at least one of its nodes is on the boundary of

one of the grains in the neighborhood $n - 1$. An illustration of a critical grain and its first two neighborhoods is shown in Fig. 9.

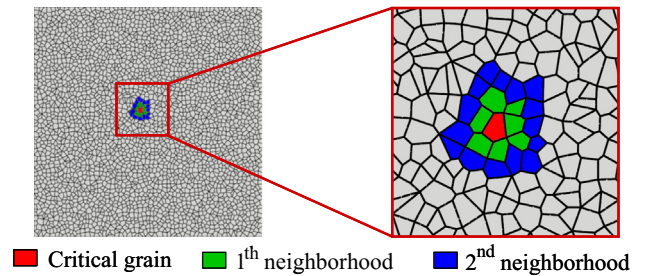


Fig. 9. Example of a critical grain and its two first neighborhoods.

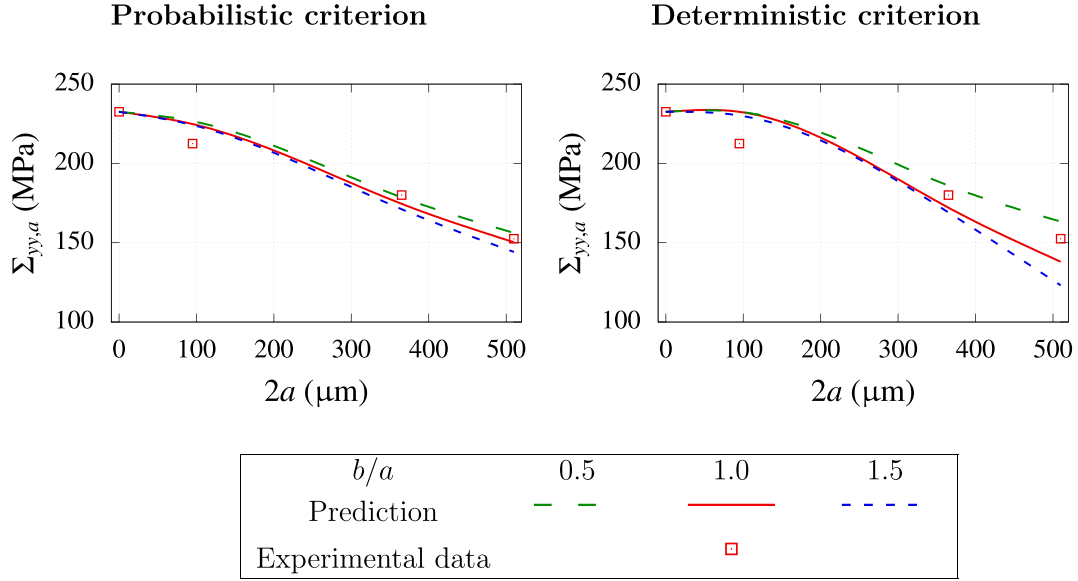


Fig. 10. Fatigue limits determined experimentally and predicted by the criteria as a function of defect size $2a$ for different ellipse aspect ratios b/a .

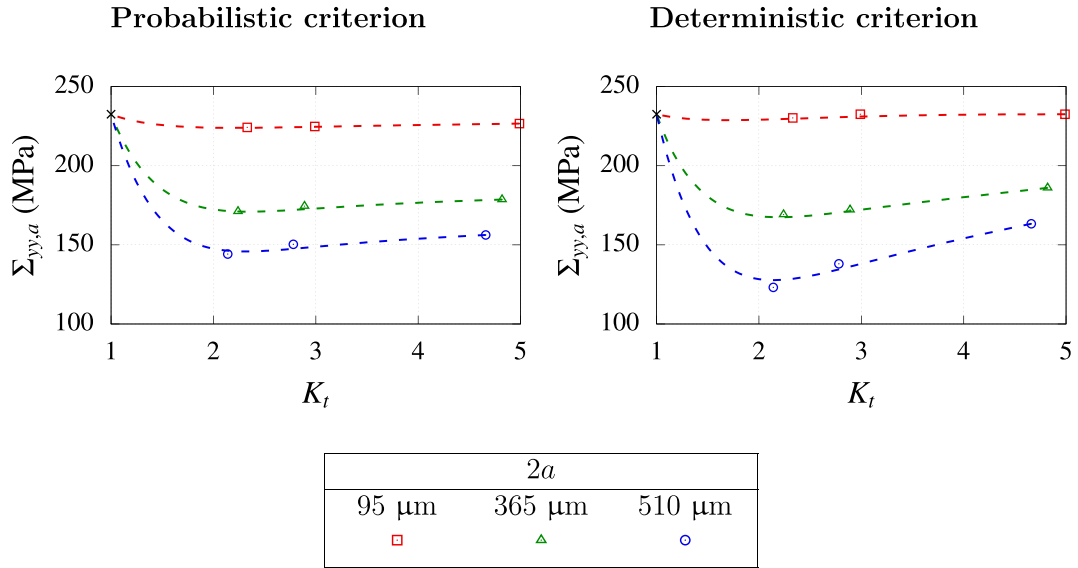


Fig. 11. Fatigue limits evaluated through the two criteria as a function of the stress concentration K_t for different defect sizes $2a$.

4.2. Calibration of the fatigue criteria

The calibration of four parameters is required for each criterion:

- a and α which describe the detrimental effect of $\sigma_{n,a}(\underline{n})$ on the fatigue strength,
- b and β which characterize the sensitivity of the fatigue limit to $\sigma_{n,m}(\underline{n})$,
- τ'_0 and γ which are related to the fatigue limit in terms of $\tau_a(\underline{n})$,

- m and N_n which allow to weight the effect of a notch on the fatigue strength.

The results from the FEA of microstructures loaded at the average fatigue limit level, in different loading conditions, are required to calibrate these parameters. The loading conditions, applied on the unnotched polycrystal and selected to obtain various distributions of the local stress states, are the fully reversed uniaxial tension, the fully reversed shear and the uniaxial tension with a stress ratio $R_\sigma = 0.1$. In the case of the probabilistic criterion, the

Table 4
Parameters of the probabilistic and deterministic fatigue criteria for a 316L steel.

| Probabilistic criterion | | | | Deterministic criterion | | | |
|-------------------------|----------------------|-----------------|-----|-------------------------|----------------------|----------------|-------|
| a | b | τ'_0 (MPa) | m | α | β | γ (MPa) | N_n |
| $1.98 \cdot 10^{-1}$ | $2.33 \cdot 10^{-3}$ | 535 | 6 | $2.14 \cdot 10^{-1}$ | $3.10 \cdot 10^{-1}$ | 130 | 14 |

parameter m is imposed and the remaining parameters are calibrated such that the failure probability of the polycrystal P_{Fa} is, in average on the 10 different realizations of microstructure, equal to 0.5 for each of the three loading conditions.

Similarly, the parameter N_n of the deterministic criterion is imposed and the remaining parameters are calibrated such that the weighted equivalent stress $\sigma_{eq,w}$ is, in average on the 10 different realizations of microstructure, equal to γ for each of the three loading conditions.

The values of m and N_n are chosen so that the fatigue limits evaluated in fully reversed uniaxial tension, for $b/a = 1.0$ and the three defect sizes $2a$, are as much as possible in accordance with those determined experimentally. The values obtained for the parameters are shown in Table 4.

4.3. Predictions of the fatigue criteria

The fatigue criteria are then used to estimate the average fatigue limits for the other geometries of elliptical hole studied. For a given ratio b/a and defect size $2a$, the average fatigue limit is evaluated by determining the macroscopic stress amplitudes $\sigma_{yy,a}$ which have to be applied to the matrix such as, in average on the 10 realizations:

- P_{Fa} is equal to 50% in the case of the probabilistic criterion,
- $\sigma_{eq,w}$ is equal to γ in the case of the deterministic criterion.

The predictions obtained for each criterion are displayed, along with the experimental data, in a diagram representing the average fatigue limit $\Sigma_{yy,a}$ against the defect size $2a$ (see Fig. 10). It can be observed that both criteria satisfactorily predict the detrimental effect of a circular hole on the fatigue limit in fully reversed tension. Indeed, the maximum differences observed do not exceed 6% in the case of the probabilistic criterion and 10% in the case of the deterministic criterion. Moreover, the ellipse aspect ratio b/a does not affect significantly the estimations of the fatigue criteria, at least for the considered ranges of defect size $2a$ and ratio b/a , especially in the case of the probabilistic criterion where the difference does not exceed 5%.

The evolution of the evaluated fatigue limit $\Sigma_{yy,a}$ as a function of the stress concentration factor K_t is illustrated in Fig. 11 for different values of defect size $2a$. The stress concentration factor K_t is defined, in the present case, as the ratio between the maximum axial stress $\Sigma_{yy,max}$, located at the notch root, and the average stress across the overall section $\Sigma_{yy,nom}$, considering a homogeneous isotropic elastic medium. The stress concentration factors K_t have been computed using the closed-form expression proposed by Tan [17] in the case of an elliptical notch in a finite-width plate.

It appears that a decrease in the stress concentration factor K_t , i.e. an increase in the ellipse aspect ratio b/a and in the curvature radius $\rho = b^2/a$ in the critical regions of the ellipse, leads to a decrease in the average fatigue limit $\Sigma_{yy,a}$. Moreover, this decrease is more perceptible for the highest values of defect size $2a$. Only a slight decrease is observed in the case of a defect size $2a = 95 \mu\text{m}$. Indeed, for both criteria, a reduction of approximately 1% is observed when the ellipse aspect ratio increases from 0.5 to 1.5. In the case of the greatest defect size, $2a = 510 \mu\text{m}$, 8% and 25% drops are predicted by the probabilistic criterion and the deterministic criterion, respectively. Without additional experimental data, it is difficult to quantitatively assess the relevance of the estimations of both criteria but at least these results are in accordance

with the experimental trends observed by Billaudeau et al. [10] in the case of notches with stress concentration factors ranging from 2 to $+\infty$ (see Fig. 1).

5. Conclusions

The mechanical state at the grain scale in polycrystals containing an elliptical hole and loaded in fully reversed tension has been obtained thanks to finite element analysis. A significant variability of stress fields, caused by the different configurations of crystalline orientations in addition to the anisotropy of the local mechanical behavior, is observed from these results. Moreover, among the notable characteristics of the mechanical response, it has been shown that the scatter of the stress field is larger in the vicinity of the elliptical notch than in the rest of the microstructure.

The estimations provided by the two multiaxial fatigue criteria have been compared to the experimental fatigue limits in the case of a circular hole. A good agreement has been generally observed for the examined defect sizes. Moreover, both criteria predict that a decrease in the aspect ratio of the ellipse b/a leads to a slight increase in the average fatigue limit in fully reversed tension. These evaluations are consistent with the experimental trends discussed by Billaudeau et al. in the case of a low-carbon steel, for the range of stress concentration factor analyzed.

References

- [1] Kitagawa H, Takahashi S. Fracture mechanical approach to very small fatigue crack growth and to the threshold condition. *Trans Jpn Soc Mech Eng Ser A* 1979;45(399):1289–303.
- [2] Shyam A, Blau P, Jordan T, Yang N. Effect of submillimeter size holes on the fatigue limit of a high strength tool steel. *Fatigue Fract Eng Mater Struct* 2014;37(4):368–79.
- [3] Endo M, McEvily A. Initiation stress and crack length in mild steel. *Proc Inst Mech Eng* 1959;173:811–27.
- [4] Murakami Y, Endo M. Quantitative evaluation of fatigue strength of metals containing various small defects or cracks. *Eng Fract Mech* 1983;17(1):1–15.
- [5] Endo M, McEvily A. Fatigue crack growth from small defects under out-of-phase combined loading. *Eng Fract Mech* 2011;78(8):1529–41.
- [6] Crossland B. Effect of large hydrostatic pressures on the torsional fatigue strength of an alloy steel. In: *Proc. int. conf. on fatigue of metals*. Institution of Mechanical Engineers; 1956. p. 138–49.
- [7] Nadot Y, Billaudeau T. Multiaxial fatigue limit criterion for defective materials. *Eng Fract Mech* 2006;73(1):112–33.
- [8] Leopold G, Nadot Y. Fatigue from an induced defect: experiments and application of different multiaxial fatigue approaches. *J ASTM Int* 2010;7:1–16.
- [9] Vincent M, Nadot-Martin C, Nadot Y, Dragon A. Fatigue from defect under multiaxial loading: defect stress gradient (dsg) approach using ellipsoidal equivalent inclusion method. *Int J Fatigue* 2014;59:176–87.
- [10] Billaudeau T, Nadot Y, Bezine G. Multiaxial fatigue limit for defective materials: mechanisms and experiments. *Acta Mater* 2004;52(13):3911–20.
- [11] Robert C, Saintier N, Palin-Luc T, Morel F. Micro-mechanical modelling of high cycle fatigue behaviour of metals under multiaxial loads. *Mech Mater* 2012;55:112–29.
- [12] Guerchais R, Morel F, Saintier N, Robert C. Influence of the microstructure and voids on the high-cycle fatigue strength of 316L stainless steel under multiaxial loading. *Fatigue Fract Eng Mater Struct* 2015;38:1087–104.
- [13] Guerchais R, Scalet G, Constantinescu A, Auricchio F. Micromechanical modeling for the probabilistic failure prediction of stents in high-cycle fatigue. *Int J Fatigue* 2016;87:405–17.
- [14] Geuzaine C, Remacle J-F. Gmsh: A 3-D finite element mesh generator with built-in pre- and post-processing facilities. *Int J Numer Methods Eng* 2009;79(11):1309–31.
- [15] Teklu A, Ledbetter H, Kim S, Boatner L, McGuire M, Keppens V. Single-crystal elastic constants of fe-15ni-15cr alloy. *Metall Mater Trans A* 2004;35(10):3149–54.
- [16] Méric L, Cailletaud G, Gaspérini M. F.E. calculations of copper bicrystal specimens submitted to tension-compression tests. *Acta Metall Mater* 1994;42(3):921–35.
- [17] Tan SC. Stress concentrations in laminated composites. Basel, Switzerland: Technomic Publishing AG; 1989.